Large spin-shuttling oscillations enabling high-fidelity single-qubit gates

Akshay Menon Pazhedath,[1,2,*] Alessandro David,[1] Max Oberländer,[3] Matthias M. Müller,[1]
Tommaso Calarco,[1,2,4] Hendrik Bluhm,[3,5] and Felix Motzoi[1,2,†]

[1] *Peter Grünberg Institute-Quantum Control (PGI-8), Forschungszentrum Jülich GmbH, D-52425 Jülich, Germany*
[2] *Institute for Theoretical Physics, University of Cologne, Zülpicher Straße 77, 50937 Cologne, Germany*
[3] *JARA-FIT Institute for Quantum Information, Forschungszentrum Jülich GmbH and RWTH Aachen University, Aachen, Germany*
[4] *Dipartimento di Fisica e Astronomia, Università di Bologna, 40127 Bologna, Italy*
[5] *ARQUE Systems GmbH, 52074 Aachen, Germany*

(Received 25 November 2024; revised 19 May 2025; accepted 1 August 2025; published 11 September 2025)

There have been impressive breakthroughs in semiconductor quantum dots in recent years, with single- and two-qubit gate fidelities matching other leading platforms and scalability still remaining a relative strength; however, due to qubit wiring considerations, mobile electron architectures have been proposed to facilitate upward scaling, and this opens the possibility of enlarging the motional amplitude for electric-dipole spin resonance (EDSR)-based qubit manipulation. In this work, we examine and demonstrate the possibility of significantly outperforming static-EDSR-type single-qubit pulsing by taking advantage of greater spatial mobility to achieve higher Rabi frequencies and reduce the effect of charge noise. Our theoretical results indicate that fidelities are ultimately bottlenecked by spin-valley physics, which can be suppressed through the use of quantum optimal control. We demonstrate that, across different potential regimes and competing physical models, shuttling-based single-qubit gates retain significant advantages over existing alternatives.

DOI: 10.1103/4lky-413f

I. INTRODUCTION

Spin-based devices in semiconducting heterostructures [1] are promising candidates to host and manipulate qubits [2] as they offer advantages such as an inherent two-level structure, controllability through gate-tunable electrostatic potentials, and direct interfacing with existing semiconductor technologies [3,4]. Si-SiGe heterostructures have been widely used to harbor spin qubits in quantum dots, with long spin-relaxation times (beyond seconds) [5] and dephasing times (beyond tens of microseconds) [6,7]. Moreover, there have been impressive breakthroughs in semiconductor quantum dots in recent years, with single- and two-qubit gate fidelities matching other leading platforms [8–11].

The scalability of such systems is limited by the short range of the exchange interaction, which leads to a fan-out of electrostatic gates when wiring a large number of qubits, as well as to crosstalk errors. Sparse architectures with on-chip controls [12–16] are among the possible solutions to this problem, but they require long-range coherent links between distant qubit registers. We focus here on systems in which the qubit, which is a single electron spin in a single quantum dot, is moved by a series of electrostatic gates, allowing bidirectional conveyor-mode shuttling [17–20]. In this approach, the spin is manipulated by transporting it to a dedicated zone where a micromagnet is present. The spatial separation of the operating qubits to such manipulation zones effectively reduces crosstalk errors when compared to dense qubit architectures.

Single-qubit operations of quantum-dot spins in presence of an artificial spin-orbit field have already been demonstrated [6,8,21–23]. These experiments leverage electric-dipole spin resonance (EDSR) [24], where the quantum-dot confinement potential is oscillated beneath a static micromagnet so that the spin experiences a periodic magnetic field; however, this is achieved in a setting where the amplitude of oscillation is limited to around 1 nm and, therefore, the magnetic field gradients required

*Contact author: a.pazhedath@fz-juelich.de
†Contact author: f.motzoi@fz-juelich.de

for fast gates are relatively large. Moreover, larger field gradients increase the coupling between spin and voltage noise, leading to spin dephasing. In contrast, shuttling architectures, such as the SpinBus architecture [14], are predicted to have the ability to perform larger-amplitude oscillations, up to 10 or 20 nm, weakening the gradient-field requirement by at least an order of magnitude and improving the spin-dephasing time. This can be combined with a geometry-optimized micromagnet for further improvements [25,26].

An obstacle to achieving high-fidelity gates in this context is the presence of low-lying valley states in the conduction band minimum of Si [27]. Evidence shows that these states couple to the spin degree of freedom (DOF) by having different g factors [6,28–30]. This modifies the standard fixed-frequency Rabi formula by introducing valley-dependent energy shifts, a fact that complicates controllability and may ultimately lead to decoherence. The interaction between the electron wave function and the heterostructure walls lifts the degeneracy of the valley DOF, but the splitting is very sensitive to the local atomic arrangement [31,32]. As the quantum dot is shuttled, the valley DOF may spend an undetected amount of time in its excited state, corresponding to a shift in the precession rate of the spin and to phase randomization. In the context of long-distance shuttling, various control approaches have been suggested for high-fidelity transport even in the presence of low-lying valley states [33–37].

In this work, we model the shuttling-based EDSR operation, taking into account the dephasing mechanism between spin and valley states. A conveyor-mode shuttling device is modeled by generating position-dependent valley eigenstates and eigenvalues, referred to as the valley landscape throughout this work, according to two distinct models. One model considers the presence of Ge atoms in the Si well (referred to as the "Ge-diffusion model") [31], while the other focuses on the presence of fabrication miscuts along the length of the device (referred to as the "step model") [32]. We show that the large electron oscillations increase the spin-dephasing time of the qubit while operating at a magnetic gradient an order of magnitude lower, with single-qubit gate fidelity limited by low valley splitting points <15 μeV (LVSPs) and strong spin-valley coupling. The electron trajectory can be shaped using the optimal control techniques presented in this work to improve the fidelity by at least 2 orders of magnitude, in a valley-model-agnostic manner. We study the dependence of the average gate fidelity on the driving frequency and the spatial amplitude of the trajectory to understand underlying physical effects, and we optimize over a parameter grid of pulse lengths and spatial amplitudes to show the advantage of optimal control in realizing fast high-fidelity gates. An extensive comparison of the valley models discussed above for various realistic scenarios, in terms of attainable fidelities, is also performed to elaborate on the advantages of using trajectory shaping over other methods. Our results indicate that shuttling-based EDSR is a viable and preferable way of performing single-qubit operations in semiconducting platforms.

The remainder of this paper is structured as follows. In Sec. II, we explain the relevant details of the SpinBus architecture and present the model Hamiltonian used for our simulations, along with descriptions of the different valley models considered. We follow this with a discussion on implementing the dynamics and optimization of the single-qubit operation, where we elucidate the optimal control methodology used. Section IV deals with the main results of this work, where we show the advantages of a large-amplitude-driven EDSR and compare the valley models based on the gate fidelities for a single prototypical device as well as for 1000 different sampled devices to ascertain the advantage of using optimal control in shaping electron trajectories. We discuss potential obstacles and future work in Sec. V and conclude in Sec. VI.

II. CONVEYOR-MODE SINGLE-QUBIT ROTATIONS

In this section, we model the manipulation zone of the quantum-bus architecture (see Fig. 1), and we discuss the simulation and optimization of the single-qubit operation.

A. Device architecture

In a conveyor-mode spin-shuttling device [18], a row of electric gates generates an array of quantum dots with a sinusoidal profile inside the quantum well of a Si-SiGe heterostructure. The transported qubit is encoded in the spin of a single electron trapped in one of these quantum dots. Bidirectional shuttling of the electron over around 10 μm is possible [19] with only four phase-shifted sine waves as control signals to the gates. Figure 1 illustrates such an apparatus.

Single-qubit gates are performed via EDSR at the so-called manipulation zone by oscillating the electron under an external magnetic field (approximately 20–50 mT) [14] around a magnetic gradient generated by a suitable micromagnet. In comparison, the high-fidelity gates shown by Ref. [8] apply a similar approach of using micromagnets in conjunction with electron-position oscillation to perform EDSR. The difference is in the choice of the operating regime, with a far higher external magnetic field (around 0.5 T), a magnetic field gradient an order of magnitude higher, and oscillation amplitudes an order of magnitude lower.

B. Model Hamiltonian

We build on the model presented in Ref. [35] by adding an extra term describing the artificial spin-orbit field. The computational subspace of interest is the spin of the

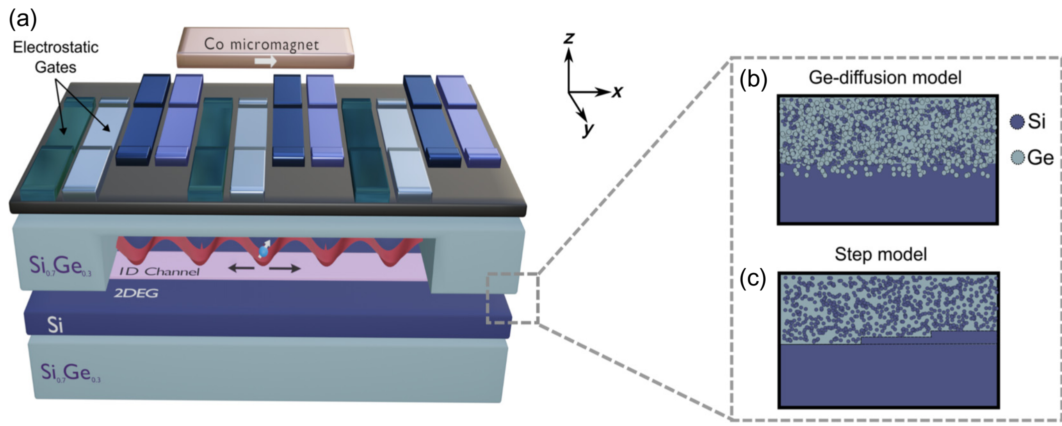

FIG. 1. Schematic of the manipulation zone in SpinBus. (a) A suitable micromagnet is placed on top of the electrostatic gates (gates of the same color receive the same phase-shifted sinusoidal signal), which enables shuttling-based single-qubit gates for the electron spin (blue ball) trapped in the Si quantum well. The trapping potential (shown in red) is moved back and forth to induce EDSR for the spin. The interface between SiGe and Si can be modeled in two different ways, as shown in (b),(c).

electron in the quantum dot, a two-level system (TLS). The spin can interact with the so-called valley DOF in Si, also a TLS [27]. The combined Hilbert space can be written as

$$\mathcal{H} = \mathcal{H}_{\text{valley}} \otimes \mathcal{H}_{\text{spin}}, \tag{1}$$

with $|+k_z\rangle, |-k_z\rangle$ as the valley basis and $|0\rangle, |1\rangle$ (computational basis) as the spin basis. Here, $|+k_z\rangle, |-k_z\rangle$ correspond to the two low-lying valley states after the sixfold degeneracy in the conduction band of Si is lifted by strain.

The Hamiltonian has four terms,

$$H = H_{\text{Zeeman}} + H_{\text{Rabi}} + H_{\text{valley}} + H_{\text{spin-valley}}, \tag{2}$$

where

$$H_{\text{Zeeman}} = \frac{1}{2} g \mu_B B_z \mathbb{1} \otimes \sigma_z, \tag{3}$$

in which g is the Landé g factor of the electron ($g = 2$), μ_B is the Bohr magneton, B_z is the constant external magnetic field applied across the manipulation zone, and σ_z is the z Pauli matrix acting on the spin. The value of B_z was chosen to be 20 mT in this work. The drive term,

$$H_{\text{Rabi}} = \frac{1}{2} g \mu_B B_x(x_{\text{qd}}(t)) \mathbb{1} \otimes \sigma_x, \tag{4}$$

corresponds to the perpendicular magnetic field $B_x(x_{\text{qd}}(t)) = \partial b_\perp \cdot x_{\text{qd}}(t)$ due to micromagnets, which is responsible for Rabi driving. Here, σ_x is the x Pauli matrix acting on spin and $x_{\text{qd}}(t)$ is the position of the center of the quantum dot at time t. The value of $\partial b_\perp$ for the SpinBus is typically chosen to be 0.1 mT/nm. We first consider the position of the electron varying as a simple sine wave given by

$$x_{\text{qd}}(t) = x_0 \sin(\omega t + \phi), \tag{5}$$

with x_0, ω, and ϕ denoting the amplitude, frequency, and phase of the oscillation, respectively. The SpinBus architecture provides dynamic control over the position x_{qd} of the trapping potential, using the same finger gates responsible for shuttling the electron through the device, which directly translates into spatial control of the electron trapped inside the potential well. Here, H_{Zeeman} causes precession of the spin around the quantization axis, and H_{Rabi} acts perpendicular to the quantization axis to rotate the spin in the preferred direction. The choice of the phase in Eq. (5) gives the usual σ_x and σ_y gates in the rotating frame. Rabi oscillations occur between the spin-up and spin-down states due to EDSR, with the frequency

$$\omega_{\text{Rabi}} = g \mu_B \partial b_\perp x_0 / \hbar, \tag{6}$$

which is modified as $\Omega = \sqrt{\delta^2 + \omega_{\text{Rabi}}^2}$, where δ is the detuning from the spin-splitting frequency. In general, the valley Hamiltonian can be expressed as

$$H_{\text{valley}} = \Delta_{\text{real}}(x_{\text{qd}}(t))\tau_x + \Delta_{\text{imag}}(x_{\text{qd}}(t))\tau_y, \tag{7}$$

where τ_x and τ_y are Pauli operators in the valley subspace, and $\Delta_{\text{real}}(x_{\text{qd}}(t))$ and $\Delta_{\text{imag}}(x_{\text{qd}}(t))$ correspond to the real and imaginary parts of the complex position-dependent intervalley coupling, respectively. The magnitude of valley splitting is given by $E_V(x_{\text{qd}}) = 2\sqrt{\Delta_{\text{real}}^2(x_{\text{qd}}(t)) + \Delta_{\text{imag}}^2(x_{\text{qd}}(t))}$, and the valley phase is given by $\varphi_V = \arg(\Delta_{\text{real}}(x_{\text{qd}}(t)) + i\Delta_{\text{imag}}(x_{\text{qd}}(t)))$. The values of $\Delta_{\text{real}}(x_{\text{qd}}(t))$ and $\Delta_{\text{imag}}(x_{\text{qd}}(t))$ are generated according to two different models for the microscopic valley physics [see Figs. 1(b) and 1(c), respectively]. The first is the Ge-diffusion model [31] which considers the microscopic arrangement of Ge atoms inside the Si well, leading to larger or smaller valley splittings depending on the overlap of the electron wave function with Ge atoms. In this work, we use the same adaptation of the Ge-diffusion model that can be found in Ref. [35].

The second valley model is the so-called step model, which is a legacy model introduced as an early interpretation of valley-splitting fluctuations [32]. With appropriate parameters, it results in a different distribution of valley-splitting values when compared to the Ge-diffusion model, and we adopt it here to study the effect of different statistics for the valley DOF, matching mean and standard deviation.

The step model assumes that the shuttling device can be divided into regions with smooth and uniform walls such that the valley Hamiltonian is constant inside the region. Changes to the valley Hamiltonian happen only at the regions' interfaces, and the effective intervalley coupling is the average of the regions' intervalley couplings weighted by the probability of the wave function being inside that region. Assuming, for simplicity, that the region interfaces are perpendicular to the direction of motion, and indicating the borders of the jth region as $[x_{j-1}, x_j]$, we compute the probability of finding the electron in this region as

$$p_j(t) = \mathrm{CDF}\left(\frac{x_j - x_{\mathrm{qd}}(t)}{\sigma_{\mathrm{qd}}}\right) - \mathrm{CDF}\left(\frac{x_{j-1} - x_{\mathrm{qd}}(t)}{\sigma_{\mathrm{qd}}}\right), \tag{8}$$

where $\mathrm{CDF}((x-\mu)/\sigma) = (1 + \mathrm{erf}((x-\mu)/(\sigma\sqrt{2})))/2$ is the cumulative distribution function of a normal distribution with mean μ and standard deviation σ, and erf is the error function. The intervalley coupling is therefore

$$\Delta = \sum_j p_j(t)\Delta_j = \sum_j p_j(t)|\Delta_j|(\cos(\varphi_{V,j}) + i\sin(\varphi_{V,j})). \tag{9}$$

The last term in the Hamiltonian is a position-dependent effective ZZ interaction between the valley and spin DOF, given by

$$H_{\text{spin-valley}} = -\kappa_z\left(\tilde{\tau}_z(x_{\mathrm{qd}}) \otimes \sigma_z\right), \tag{10}$$

where κ_z is typically chosen to be of the order of 1×10^{-6} to 5×10^{-6} meV, which is proportional to the relative g-factor variation $\delta g/g \approx 10^{-3}$ [30,38]. Here, $\tilde{\tau}_z(x_{\mathrm{qd}}) = \{\cos(\varphi_V(x_{\mathrm{qd}}))\tau_x + \sin(\varphi_V(x_{\mathrm{qd}}))\tau_y\}$ is the z Pauli matrix acting on the ground and excited states of valley, and $\varphi_V(x_{\mathrm{qd}})$ is the valley phase at a chosen starting position.

III. DYNAMICS AND OPTIMIZATION

The combined spin-valley system follows open system dynamics, with the valley DOF decaying in contact with the crystal environment and the spin DOF dephasing because of charge noise. The density matrix of the combined system, $\rho(t)$, evolves according to the master equation

$$\frac{\mathrm{d}\rho}{\mathrm{d}t}(t) = -\frac{i}{\hbar}[H\left(x_{\mathrm{qd}}(t)\right), \rho(t)] + \frac{1}{T_{1,v}}\mathcal{D}\left[\tilde{\tau}_-\left(x_{\mathrm{qd}}(t)\right)\right](\rho(t)) + \frac{1}{T_{2,s}}\mathcal{D}[\sigma_z](\rho(t)), \tag{11}$$

where we have the dissipative operator $\mathcal{D}[L](\rho) = L\rho L^\dagger - (\rho L L^\dagger + L L^\dagger \rho)/2$, $T_{1,v} = 100$ ns (corresponding to valley decay), and $T_{2,s} = 20$ to $80\,\mu$s (corresponding to spin dephasing). The jump operator used for the valley relaxation is given by [35]

$$\tilde{\tau}_-(x_{\mathrm{qd}}) = \frac{1}{2}\begin{pmatrix} 1 & e^{-i\varphi_V(x_{\mathrm{qd}})} \\ -e^{i\varphi_V(x_{\mathrm{qd}})} & -1 \end{pmatrix}, \tag{12}$$

which is the lowering operator from the local valley excited state to the local valley ground state.

A. GRAPE with JAX

The shuttling path, or the trajectory of the electron as shown in Eq. (5), is discretized into piecewise-constant functions, as in the usual approach of the well-known GRAPE algorithm [39]. The time step is chosen so as to capture the relevant spin-valley dynamics, and this is calculated to be around 0.8 ps from the average valley splitting along the length of the device. The discretized trajectory is used to perform state evolution, and finally, the average gate fidelity is calculated as explained in Sec. III C. Performance improvements for state evolution and fidelity evaluation are achieved using the JAX library in PYTHON [40]. This also enables autodifferentiation of the cost function, which is essential for backpropagating the errors to perform the optimization. The gradients found using autodifferentiation are used with the L-BFGS optimization method in SCIPY [41] to minimize the average gate infidelity $(1-\bar{F})$. The optimization is carried out with fewer controls (fixed to ten controls per nanosecond) than the time-discretized steps, and it is then interpolated when calculating the final gate fidelity [42].

B. Shaping function

The initial control pulse is sinusoidal, as in Eq. (5). To ensure that the pulse starts and ends at the same point, we shape it using a Gaussian ramp envelope, given as

$$G(t) = \begin{cases} f_s(t - t_r) & \text{if } t \le t_r, \\ 1 & \text{if } t \ge t_r \wedge t \le T_g - t_r, \\ f_s(\tilde{t} + t_r) & \text{if } t \le T_g - t_r, \end{cases} \tag{13}$$

where $f_s(t) = \alpha[\exp(-\tilde{t}^2/2\sigma^2) - \exp(-t_r^2/2\sigma^2)]$, with $\tilde{t} = t - t_f$, $\sigma = t_r/4$, and $\alpha = [1 - \exp(-t_r^2/2\sigma^2)]^{-1}$. Here, t_r is the rise time, set here to 1 ns, and T_g is the gate time. The shaped pulse to be optimized will be $\tilde{x}_{\mathrm{qd}}(t) = G(t) \cdot x_{\mathrm{qd}}(t)$.

C. Cost function

The function to be maximized is the average gate fidelity of the quantum channel $\mathcal{E}$, evolving an initial spin state according to Eq. (11) and subsequently tracing out the valley DOF, compared to a desired unitary U. We use

$$\bar{F}(\mathcal{E}, U) = \frac{dF_{\mathrm{ent}}(\mathcal{E}, U) + 1}{d+1}, \tag{14}$$

as defined in Ref. [43], with $d = 2$. Here, $F_{\mathrm{ent}}(\mathcal{E}, U)$ is the entanglement fidelity and is denoted by $F_{\mathrm{ent}}(\mathcal{E}, U) = \langle\phi|\,(\mathbb{1} \otimes \mathcal{U}^{\dagger} \circ \mathcal{E})(\phi)\,|\phi\rangle$, where $|\phi\rangle$ is a maximally entangled state of the spin with an ancilla qubit and $\mathcal{U}^{\dagger}(\rho) = U^{\dagger}\rho U$. In practice, the calculation of $F_{\mathrm{ent}}(\mathcal{E})$ involves the propagation of four initial spin states (see for example Ref. [35]). We note that the coherent and incoherent errors might be weighted differently [44] if there is significant leakage into valley states, given that we are using the average gate fidelity as a figure of merit. Nonetheless, with optimal control, the coherent errors are explicitly suppressed, effectively lifting the quadratic relationship on coherent error.

For our simulations, the target gate U_G was chosen to be a rotation of π about the y axis, given by

$$U_G = \exp\left(-i\pi\sigma_y/2\right). \tag{15}$$

Note that there is no constraint against choosing U_G as any other desired gate. As the simulated evolution in Eq. (11) is in the lab frame, the spin precesses under the action of H_{Zeeman} and $H_{\mathrm{spin\text{-}valley}}$, in addition to the desired gate. In the ideal case of the electron always remaining in the valley ground state throughout the evolution, the frequency of precession is $\hbar\Omega_R = 2\mu_B B_z + 2\kappa_z$. We counter-rotate the final spin state to transform into a precession-free rotating frame via $U_R = \exp(-i\Omega_R\sigma_z)$. Finally, in Eq. (14), we use $U = U_R U_G$, which ensures that the optimizer will favor the trajectory that keeps the electron in the valley ground state.

IV. RESULTS

This section is divided into three parts. We first compare shuttling-based EDSR with static EDSR by relating the influence of transverse magnetic field gradients on spin dephasing and average gate fidelity. Next, we investigate the spin-valley interplay mechanism and the use of optimal control as a means to perform high-fidelity gates for driving pulses with various amplitudes and durations. Finally, we show the differences in single-qubit gate fidelity for competing valley models. Device-specific and ensemble-averaged gate fidelities are analyzed to understand the limitations imposed by spin-valley decoherence.

A. Static versus shuttled quantum dots: Effect on spin dephasing

Static quantum dots in a Si-SiGe heterostructure have achieved high-fidelity single-qubit operations using micromagnet-enabled EDSR, with $T_2^* = 20\,\mu\mathrm{s}$ [8], while operating in the regime mentioned in Sec. II A. EDSR based on lower amplitudes limits the achievable gate time, resulting in slower gates. In principle, a larger x_0 value combined with large $\partial b_{\perp}$ could lead to faster gates, but keeping small gradients reduces the effects of charge noise.

Charge noise arising from voltage fluctuations in confinement potentials is transferred to the spin as dephasing noise by the longitudinal component of the magnetic gradient, $\partial b_{\parallel}$. This reduces the T_2^* value of a device, which is reported in Ref. [46] as $T_2^* = \hbar\sqrt{2}/(g\mu_B\delta B_{\mathrm{rms}})$, where $\delta B_{\mathrm{rms}} = \partial b_{\parallel}\delta x_{\mathrm{rms}}$ is the root-mean-square (rms) variation of magnetic field and δx_{rms} denotes the rms displacement of the electron position x_{qd} caused by voltage fluctuations (see Ref. [8] supplementary). This yields

$$T_2^* = \frac{\hbar\sqrt{2}}{g\mu_B\partial b_{\parallel}\delta x_{\mathrm{rms}}}. \tag{16}$$

Changing the geometry of the micromagnet can maximize the ratio $Q = \partial b_{\perp}/\partial b_{\parallel}$ between transverse and longitudinal gradients to improve the T_2^* value of a device [26]. Although design dependent, the maximum and minimum values of Q are generally finite and typically span about one order of magnitude. It follows that the choice of transverse gradient used for EDSR will influence spin dephasing. Substituting $\partial b_{\parallel} = \partial b_{\perp}/Q$ in Eq. (16), we obtain

$$T_2^* = \frac{Q\hbar\sqrt{2}}{g\mu_B\partial b_{\perp}\delta x_{\mathrm{rms}}} = \frac{QT_g x_0\sqrt{2}}{\pi\,\delta x_{\mathrm{rms}}}, \tag{17}$$

directly relating T_2^* with Q as well as the amplitude of oscillations x_0 and the analytical gate time T_g, which is computed as

$$T_g = \frac{\pi}{\omega_{\mathrm{Rabi}}} = \frac{\pi\hbar}{g\mu_B\partial b_{\perp}x_0}. \tag{18}$$

We estimate $\delta x_{\mathrm{rms}} = 2\,\mathrm{pm}$ from the analysis of Ref. [8] (supplementary) as well as by matching the value of T_2^* in Eq. (16) with the experimental value of 20 μs from Ref. [8]. The quantum dot is operated at $\partial b_{\perp} = 1\,\mathrm{mT/nm}$ and $\partial b_{\parallel} = 0.2\,\mathrm{mT/nm}$. To study the effect of $\partial b_{\perp}$ on T_2^*, we relate these quantities by fixing $Q = 5$. In the case of EDSR by shuttling, as one reaches amplitudes an

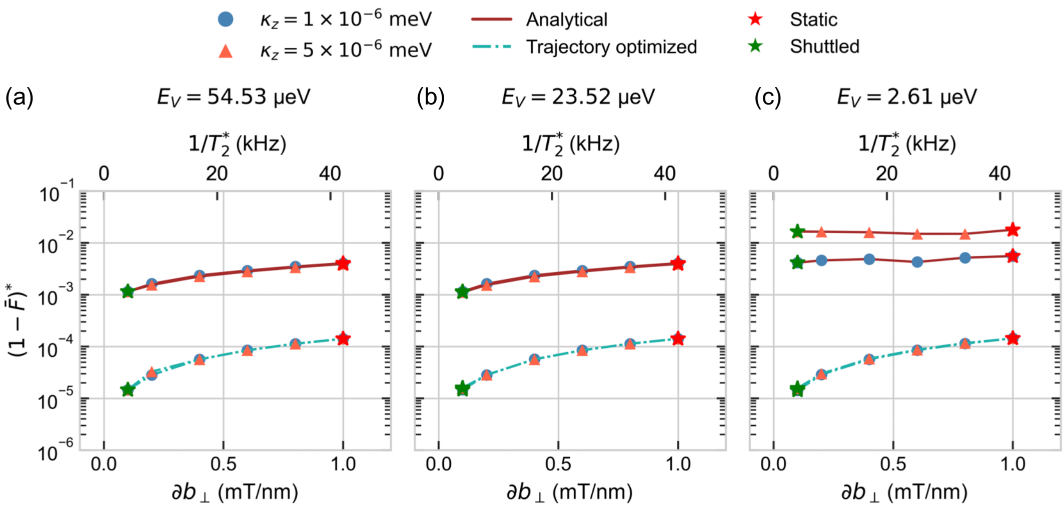

FIG. 2. Effect of transverse magnetic gradient on spin dephasing and average gate fidelity for varying valley splittings. The Ge-diffusion model is used to generate a prototypical device, and three points along the device are sampled. Pulses with varying x_0 (and corresponding analytical T_g) are used to obtain the average gate infidelity $(1-\bar{F})$ at each point. The minimum of $1-\bar{F}$ with respect to x_0 (indicated by $*$), for varying $\partial b_\perp$ and corresponding spin-dephasing rates are plotted here. (a),(b) A large valley splitting helps to retain good fidelity as the spin-dephasing rate increases (red line). (c) An LVSP combined with large spin-valley coupling leads to an average gate fidelity that is an order of magnitude worse (red line with triangles). In all cases, the advantage of shuttling the qubits over operating them statically can be seen by comparing their infidelities, as indicated by the green ($\partial b_\perp = 0.1$ mT/nm) and red ($\partial b_\perp = 1$ mT/nm) stars, respectively [45]. Irrespective of the competing physical mechanisms causing decoherence, optimal control always converges below 10^{-3}, with a significant advantage from shuttling (teal dash-dot line).

order of magnitude higher, the transverse gradient can be $\partial b_\perp = 0.1$ mT/nm [18], and therefore we assume $\partial b_\parallel = 0.02$ mT/nm. We use the Ge-diffusion model to generate a valley landscape, and we base our study on two different spin-valley couplings, specifically $\kappa_z = 10^{-6}$ meV (typically expected value [30]) and $\kappa_z = 5\times10^{-6}$ meV. Three points are sampled from this valley landscape, corresponding to valley splittings of 54.53, 23.52, and 2.61 μeV. For each point, $\partial b_\parallel$ is varied from 0.02 to 0.2 mT/nm, yielding the corresponding $\partial b_\perp$ and T_2^* [see Eq. (16)]. It follows from Eq. (6) that the Rabi frequency is directly proportional to $\partial b_\perp x_0$. For each value of $\partial b_\perp$, we vary the analytical T_g from 5 to 360 ns to generate electron trajectories with the corresponding analytical x_0 value and calculate the average gate infidelity. From this, the minimum of the infidelity, $(1-\bar{F})^*$, with respect to x_0 is calculated (Fig. 2, brown solid line). The same procedure is repeated for optimized electron trajectories (as explained in Sec. III) corresponding to each T_g and x_0 value (Fig. 2, teal dash-dot line).

The following observations are in order. First, smaller magnetic gradients result in smaller spin-dephasing rates for relatively larger values of valley splitting, as shown by the brown solid lines in Figs. 2(a) and 2(b). The advantage of smaller gradients wanes at significantly lower valley splitting, highlighting the importance of spin-valley physics at larger amplitudes, as shown in Fig. 2(c). The effect of larger spin-valley couplings becomes noticeable only in the case of small valley splitting. Second, optimal control of electron trajectories ensures an average gate infidelity below 10^{-3}, irrespective of the magnitude of the valley splitting or spin-valley coupling, for all magnetic gradients.

B. Dependence of average gate fidelity on pulse parameters

Electron trajectories can be engineered for a variety of amplitudes (x_0), frequencies (ω), and pulse lengths (T_g). To study how the system responds to these different parameters, a Ge-diffusion-model-based device is used to create a well-defined valley landscape, with $\kappa_z = 5\times10^{-6}$ meV and $E_V = 103 \pm 49$ μeV. An LVSP for which the valley splitting is approximately 7 μeV is chosen along the length of the device for Rabi pulsing to demonstrate the advantage of optimal control. The micromagnet configuration chosen in Ref. [14] is predicted to limit the maximum amplitude of oscillations to 20 nm to perform EDSR. Sweeping the values of ω for x_0 up to 20 nm, we calculate the average gate infidelity in the absence and presence of spin-valley coupling, as shown in Figs. 3(a) and 3(b), respectively. Figure 3(a) shows the case where $\kappa_z = 0$ meV, with optimal fidelities obtained for $\omega \sim 560$, corresponding to an external field of $B_z = 20$ mT. Increasing the spin-valley coupling to $\kappa_z = 5\times10^{-6}$ meV [Fig. 3(b)] produces a shift in resonant ω (to around 562.3), leading to optimal fidelities. The well-known

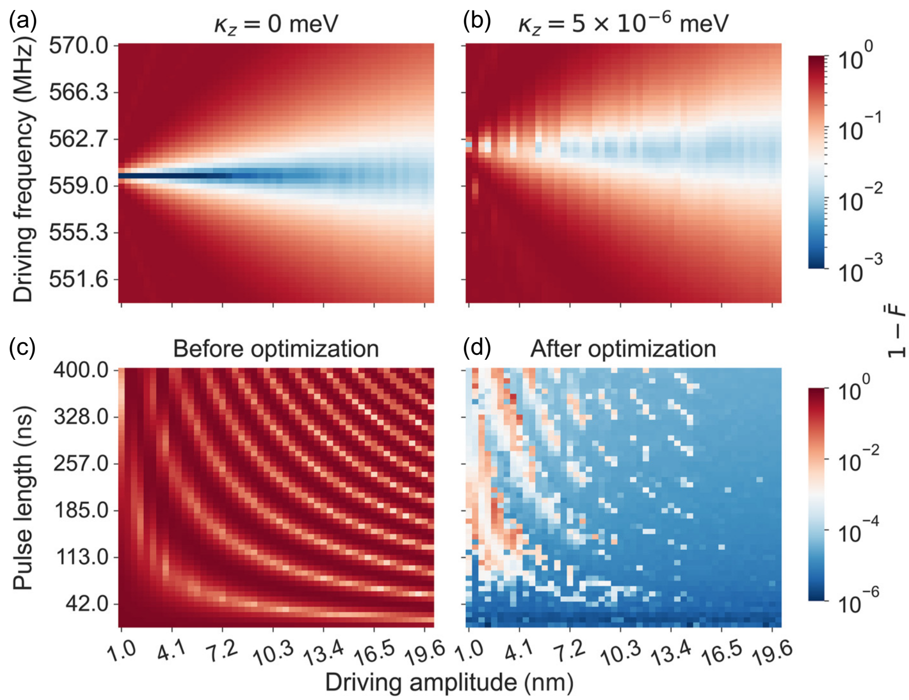

FIG. 3. Trajectory parameters and optimization. The amplitude of the driving pulse is swept along with the (a),(b) driving frequency and (c),(d) pulse length to calculate the average gate infidelity for a device simulated using the Ge-diffusion model with spin-valley coupling $\kappa_z = 5 \times 10^{-6}$ meV. (a) The case with no spin-valley coupling. When the driving frequency is closer to the spin-splitting frequency, higher fidelity is achieved. In the presence of spin-valley coupling, the spin-splitting frequency is modified (visible from the upward shift), and Landau-Zener-Stückelberg-Majorana (LZSM) interference of valley excited states leads to fringes, as shown in (b). The distinctive Chevron patterns are visible in (c), with no parameter combinations yielding infidelities below 10^{-3} before optimization. Pulses obtained through optimal control perform better at preserving the average gate fidelity, minimizing infidelities to well below 10^{-3}, as shown in (d).

Landau-Zener-Stückelberg-Majorana (LZSM) interference [47], which causes phase accumulation between the excited and ground states when passing an anticrossing point in energy periodically, occurs in the valley DOF. A strong spin-valley coupling results in fringes along the frequency band. The fringes are predominant for amplitudes <10 nm, suggesting that valley excitations are less significant at larger amplitudes.

A sweep of x_0 and T_g is also performed, and the entire parameter grid is optimized, as mentioned in Sec. III, for 300 iterations. Figure 3(c) shows the parameter grid before optimization, with no parameter combination yielding the desired fidelities. Fringes due to LZSM interference are visible at lower amplitudes, as noted above. The right-hand panel, Fig. 3(d), shows the same parameter grid after trajectory optimization, leading to 88.68% of the parameter grid yielding infidelity below 10^{-3}, highlighting the potential improvement from using optimal control. For all amplitudes, pulse lengths <42 ns resulted in high-fidelity gates. Meanwhile, driving amplitudes >14 nm yielded high-fidelity gates for all pulse lengths. This suggests that, even though there is a wide range of parameters for which the optimal control performs better, specific ranges of amplitudes and pulse lengths are more desirable when optimizing the average gate infidelity. Moreover, we note that there are a few relatively red points remaining in the parameter grid that did not yield optimal fidelities. This is primarily due to the inverse relationship between the driving amplitude and the gate time, which limits the fidelity of certain parameter combinations. After optimization, we still find these red points, and this could be due the presence of local minima in the cost landscape near the problematic parameter combinations.

C. Valley-model-agnostic optimal control

Valley models are differentiated by the choice of sampling the real and imaginary parts of the complex-position-dependent valley splitting, as mentioned in Sec. II. Ge-diffusion and step models of valley splitting can be used to simulate different functional distributions. This section is divided into two parts. The first part deals with the positioning of the micromagnet along the length of the device, and the second part deals with sampling valley profiles of 1000 different devices. In both parts, we show that very low average gate infidelities can be obtained, irrespective of the valley model used. In particular, optimal control always ensures trajectories that

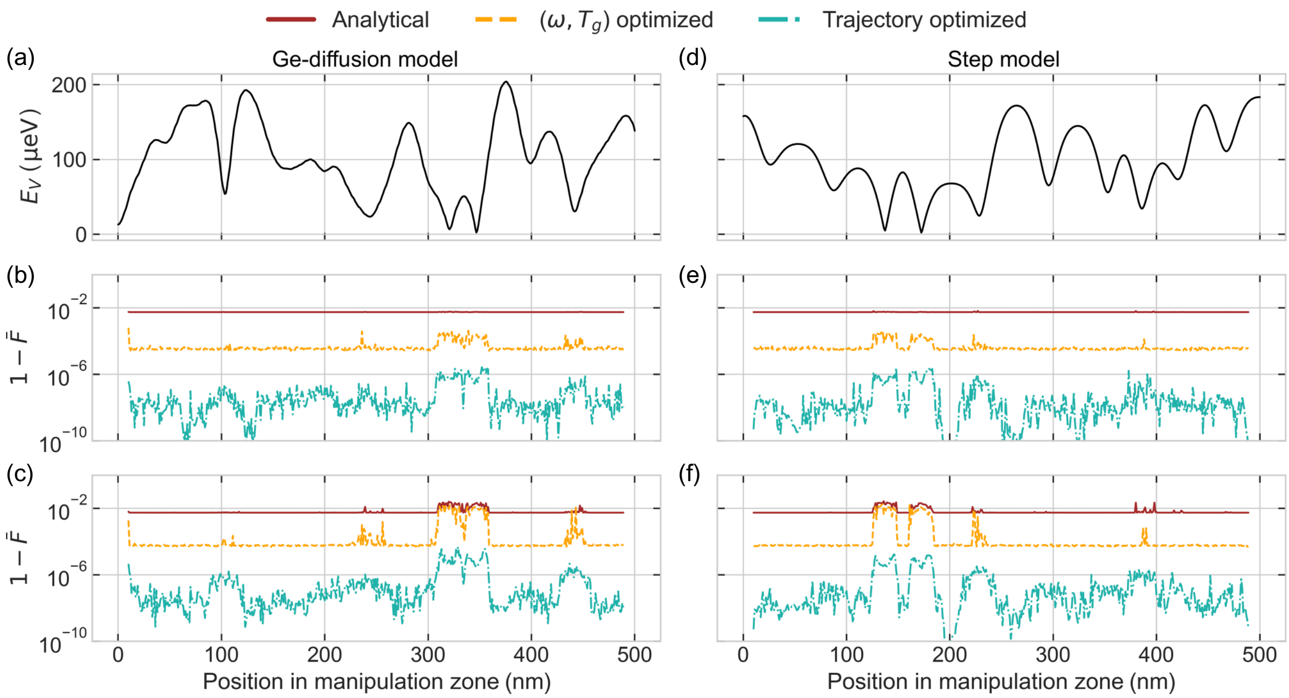

FIG. 4. Dependence of average gate fidelity on micromagnet position in the manipulation zone. For a device simulated using the Ge-diffusion model, the position of the micromagnet is varied over a chosen length. (a) Dependence of valley splitting on position. Corresponding to the valley splitting in (a), we calculate the (b) analytical [see Eq. (18)] (brown line), (ω, T_g)-optimized (orange dashed line), and trajectory-optimized (teal dash-dot line) infidelity as a function of position, for $\kappa_z = 10^{-6}$ meV. As the valley splitting decreases, the infidelity increases and becomes worse when it encounters an LVSP. Optimal control improves the average gate fidelity even at hard-to-navigate LVSPs. (c) For $\kappa_z = 5 \times 10^{-6}$ meV, this effect is enhanced for the analytical and (ω, T_g)-optimized lines, while optimal control succeeds in retaining high fidelity. (d)–(f) The same for the step model of valley splitting.

result in high-fidelity single-qubit gates for the SpinBus architecture.

1. Micromagnet-position dependence

A prototypical device is simulated using both valley-splitting models, with $\kappa_z = 10^{-6}$ meV and $\kappa_z = 5 \times 10^{-6}$ meV. In a realistic scenario, Figs. 4(a) and 4(d) show the valley landscapes for the Ge-diffusion and step models, respectively. At each point along the valley landscape, a sinusoidal electron trajectory with amplitude $x_0 = 10$ nm and corresponding analytical T_g [see Eq. (18)] at driving frequency $\omega \sim 562.3$ MHz is used to calculate average gate infidelity. Empirically, tuning ω to account for shifts due to spin-valley dynamics, and tuning T_g to correct any over- or under-rotation of the spin while performing the desired gate, could improve the average gate fidelity in experiments. In a real experiment, calibration of ω and T_g could be done independently to find the sweet spot for attaining larger gate fidelities. This process is numerically simulated using Bayesian optimization based on Gaussian processes [48], implemented in the PYTHON library SCIKIT-OPTIMIZE [49]. This method is faster than brute-force parameter sweeps for calibration because we start the optimization in a well-defined initial interval around ω_{Rabi} and analytical T_g. Conservatively, fidelities in a real experiment might fall between the analytical and Bayesian-optimized distributions due to limitations in the precision of evaluating fidelities for the respective valley splittings. Furthermore, the initial trajectory based on analytical T_g is optimized as discussed in Sec. III.

The results of optimization for the Ge-diffusion and step models corresponding to $\kappa_z = 10^{-6}$ meV are shown in Figs. 4(b) and 4(e), and those corresponding to $\kappa_z = 5 \times 10^{-6}$ meV are shown in Figs. 4(c) and 4(f), with the red solid lines denoting the analytical infidelity, the orange dotted lines denoting the (ω, T_g)-optimized infidelity, and the teal dash-dot lines denoting the trajectory-optimized infidelity. It is observed that the gate infidelities are valley-landscape dependent, which makes it important to choose an appropriate operating point for placing the micromagnet to increase the probability of performing a high-fidelity single-qubit operation in SpinBus. As noted in Sec. IV A, larger values of valley splitting inherently help achieve high fidelities, even in the presence of an unfavorable spin-valley coupling. This is evident from the flat profile of the (ω, T_g)-optimized infidelity at larger valley-splitting values, irrespective of the spin-valley coupling strength.

It can also be noted that the gradient of valley splitting with respect to position works in conjunction with the valley splitting strength to decrease average gate fidelity [for instance, between 200 and 300 in Fig. 4(c)], due to LZSM interference. Spin decoherence due to LVSPs is more prevalent at larger spin-valley couplings. The difference in the valley models chosen does not appear to change the analytical and postoptimization fidelity characteristics. Calibrating ω and T_g might suffice to provide competitive fidelities for a vast majority of points along the valley landscape, as shown in Figs. 4(b)–4(f); however, trajectory optimization always allows the average gate fidelity to converge below 10^{-4} despite encountering the competing physical effects discussed above.

2. Device sampling

The valley landscape is highly variant, and it is important to gather more statistics over many prototypical devices to ascertain the advantage of using optimal control. The valley-splitting models are used to generate 1000 devices of the same length, with varying valley landscapes. We assume that the center of the micromagnet is placed exactly at the center of the 200-nm-long device (at 100 nm), which is chosen as the initial point of the sinusoidal electron trajectory with amplitude $x_0 = 10$ nm.

a. Ge-*diffusion model.* As mentioned in Sec. II, a valley profile is generated by relative positioning of Ge atoms in the Si well. The presence of Ge atoms alters the intervalley coupling, causing a spatially varying difference in energy. To sample devices simulated using the Ge-diffusion model, a seed is chosen to randomly place Ge atoms along the Si well. Figure 5(a) (left-hand panel) shows the valley-splitting profile for the sampled devices. The average valley splitting at the center taken over the 1000 devices is approximately 88 ± 46 μeV, while the average splitting over the full length of the 1000 devices is approximately 88 ± 17 μeV. The distribution of valley splittings is skewed toward lower splittings, with 53.9% of

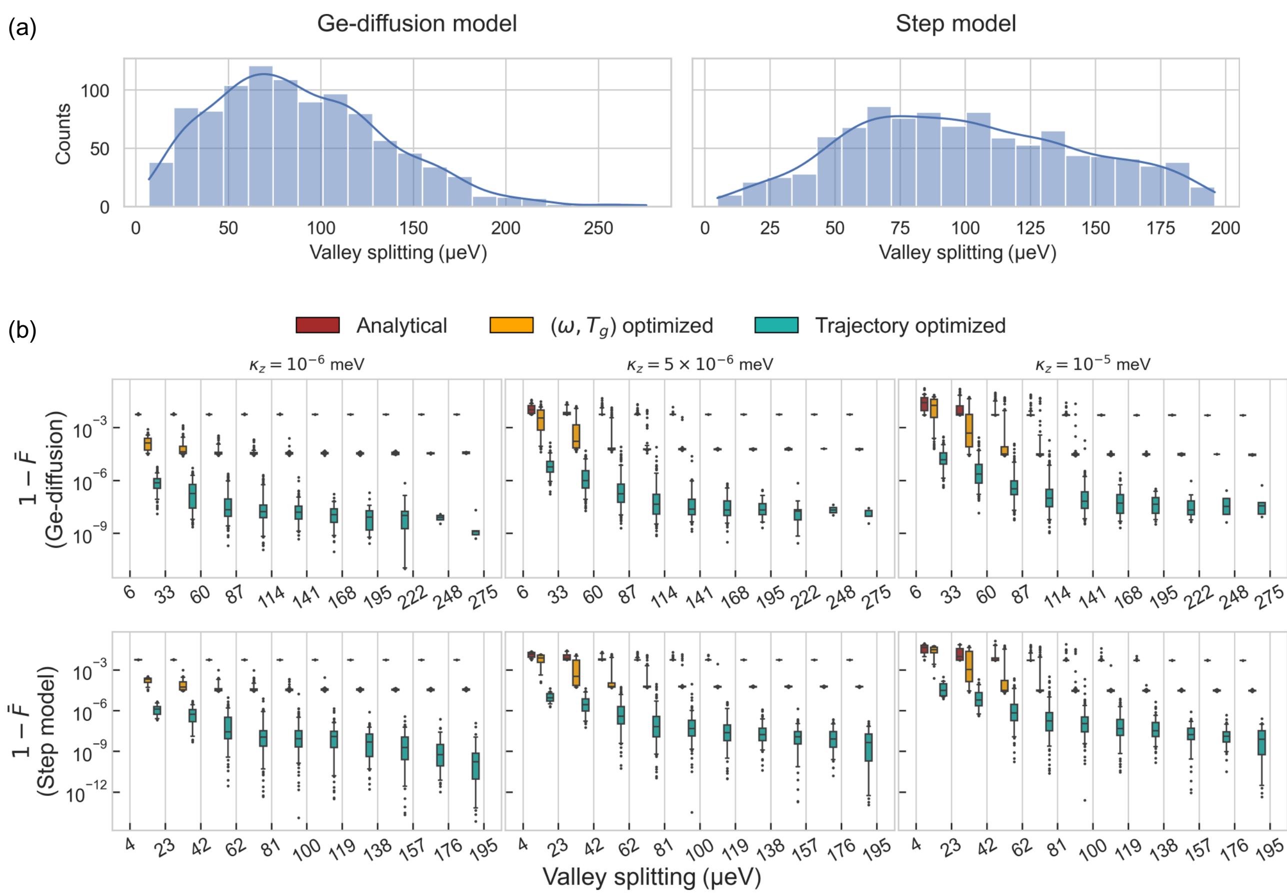

FIG. 5. Optimal control improves average gate fidelity over 1000 sampled devices. The Ge-diffusion model and the step model are used to generate 1000 different shuttling devices of 200-nm length, with varying valley-splitting distributions. (a) Valley-splitting distribution calculated at the center of each device (at 200 nm). (b) Bar plots of average gate infidelity versus valley splitting with the mean marked for the Ge-diffusion model (top row) and the step model (bottom row). Increasing spin-valley coupling leads to poor average gate fidelity for LVSPs, as shown by the analytical infidelity bars (brown). Here, (ω, T_g) optimization can improve fidelity for larger valley splittings, but this is limited by LVSPs (orange bars). Pulse engineering improves the average gate fidelity by at least 3 orders of magnitude even after encountering LVSPs (teal bars).

the samples below a splitting of 88 μeV. Valley splittings below 33 μeV are encountered with 12.3% probability.

b. Step model. The relative placement of miscuts along the device is tuned using a chosen seed so as to generate different valley profiles. The corresponding valley-splitting profile is shown in Fig. 5(a) (right-hand panel). The average valley splitting at the center is approximately 100 ± 44 μeV, while the average splitting over the full length of the 1000 devices is approximately 92 ± 15 μeV. The valley splittings are skewed more toward the larger values, with 56.6% of the samples above a splitting of 88 μeV. Valley splittings below 33 μeV are encountered with 5.6% probability, relatively less than the Ge-diffusion model. This could be attributed to lower intervalley coupling being concentrated around the step edges.

For both models, we employ the same methodology as discussed in Sec. IV C 1 to calculate analytical, (ω, T_g)-optimized, and trajectory-optimized gate infidelities, with the electron always oscillating about the center of the device for each sample. Figure 5(b) shows the results for the Ge-diffusion model (top row) and the step model (bottom row) after optimization. We observe that the analytical Rabi pulses result in poor gate fidelities as the valley splitting decreases below 60 μeV, progressively getting worse for lower valley splittings [see Fig. 5(b), brown bars]. Calibrating ω and T_g can improve the fidelity for a vast majority of samples (orange bars), but this is limited by LVSPs and relatively larger spin-valley coupling values. It can be easily seen that optimized electron trajectories perform at least 3 orders of magnitude better than the analytical Rabi pulses for all values of valley splitting.

It is evident that an important factor other than the valley splitting strength that plays a role in limiting the average gate fidelity is the spin-valley coupling. Gradually increasing the spin-valley coupling shifts the attainable infidelities upward, generally implying more spin decoherence. For $\kappa_z = 10^{-6}$ meV, none of the samples using analytical pulses converged below an average gate infidelity of 10^{-3}, while 779 (Ge-diffusion) and 899 (step model) out of 1000 samples using (ω, T_g)-optimized pulses converged below an average gate infidelity of 10^{-3}. Trajectory shaping using optimal control for the same leads to an average gate infidelity below 10^{-3} for all samples, irrespective of the underlying valley model or spin-valley coupling, posing a significant advantage over the usual Rabi pulses. In conclusion, the detrimental effects of encountering LVSPs can be effectively mitigated by optimal control.

V. DISCUSSION

Conveyor-mode shuttling-based architectures can be engineered with better spin-dephasing times than their static-quantum-dot counterparts due to their ability to perform larger amplitudes of electron-position oscillation. We have shown that for realistic spin-decoherence rates, an order-of-magnitude improvement over standard EDSR may be attainable, making the SpinBus architecture a promising candidate for scalable high-fidelity single-qubit operations, which are essential for fault-tolerant quantum computation [50–52]. Oscillating the electron at larger amplitudes increases the chance of valley excitations and position-dependent frequency offsets, thus hindering spin coherence and high-fidelity gates. The existence of LVSPs can severely limit fidelity, to the extent of making these manipulation zones unusable. In this work, we have shown that such drastic measures are unneeded, and applying optimal control still permits error rates below 10^{-3}, enabling full use of the SpinBus architecture. While we have focused here on model-based control, most of the conclusions should still hold in the case of *in situ* closed-loop control.

Meanwhile, we have shown that the valley DOF, with sufficiently large splitting (>60 μeV), does not significantly hamper the spin unless the spin-valley coupling is pessimistically large; however, appropriate calibration to account for position-dependent frequency shifts is needed. The single-qubit gate fidelities after calibration can be used to probe the unknown valley landscape along a device to map out potential LVSPs. This can guide the choice of the initial operating position of the electron to yield high-fidelity gates without the use of optimal control. Full optimal control enables high-fidelity gates even if there is a chance of encountering such spin-valley couplings in a realistic device. We have modeled both the Ge-diffusion and step-model scenarios in detail and shown that in both cases, even under pessimistic conditions, control theory can greatly enhance device operability. It is in principle also possible to engineer electron-oscillation trajectories that are inherently robust to differences in valley landscapes, as mapping out the valley landscape for large-scale devices might not be practical. Moreover, uncertainties in measuring valley splittings in an experimental scenario could be mitigated using closed-loop control techniques, allowing the trajectories to be modified in real time to yield optimal gate fidelities. Since the average number of iterations required to yield high-fidelity gates for the open-loop scheme discussed in this work is around 100, extending it to a closed-loop control scheme might increase the iterations by a factor of roughly 10 [53], which still is a break-even trade-off to achieve high-fidelity gates, especially given fast duty cycles for these devices. Energy-optimized optimal control techniques [54] could also be beneficial for addressing additional hardware power constraints along with the physical constraints of the system studied in this work.

It is also important to note that low-frequency noise, coming from nuclear spins in residual ^{29}Si or from non-Markovian effects of charge fluctuators, could cause further dephasing of the spin. This would have to be addressed with well-established methods, such as dynamical decoupling pulses [8,55]. The interplay and compatibility between dynamical decoupling pulses and the optimized pulses to avoid valley leakage suggested in our work constitute an interesting open question, which warrants further investigation.

VI. CONCLUSION

A quantum bus architecture paired with micromagnets is promising for large-scale universal quantum computation. We have quantitatively shown that an order-of-magnitude improvement over standard EDSR is possible for shuttling-based EDSR. Nonetheless, the choice of the material stack for the device (Si-SiGe in this work) presents additional complexity in the Hamiltonian and decay channels that cause decoherence of the information encoded in the spins of the electron. Higher gate fidelities are limited by the so-called valley degree of freedom arising from the conduction-band minima of Si, and they are further limited by the charge noise mediated through the micromagnets used for single-qubit manipulation.

We show that straightforward control-theoretic routines can improve the gate fidelities by at least 3 orders of magnitude compared to analytical formulas. These results are tested for two competing models for the description of valley splittings, namely the Ge-diffusion and step models. Even for valley splittings below 15 μeV, which would otherwise be essentially unusable for computation, the optimized pulses result in 99.9% gate fidelity, thus improving controllability in tough-to-navigate LVSPs that could be present along the length of the device.

ACKNOWLEDGMENTS

This work was supported by the Helmholtz Validation Fund project "Qruise" (HVF-00096) and by Germany's Excellence Strategy—Cluster of Excellence Matter and Light for Quantum Computing (ML4Q) EXC 2004/1—390534.

DATA AVAILABILITY

The data that support the findings of this article are openly available [56].

APPENDIX: OPTIMAL ELECTRON TRAJECTORIES

We discuss briefly the optimal electron trajectories obtained by following the procedure laid out in Sec. III. The valley landscape chosen is the same as the one discussed in Sec. IV B, with the initial position of the quantum dot corresponding to a valley splitting of 7 μeV. For simplicity, we choose $T_g = 50$ ns and focus on the trajectories obtained for various selected initial amplitudes, specifically $x_0 = 7.6$, 10.7, 15.3, and 20 nm. Figure 6(a) shows the optimized trajectories for each of the initial amplitudes, and the corresponding single-sided amplitude spectrum of the trajectories is plotted in Fig. 6(b).

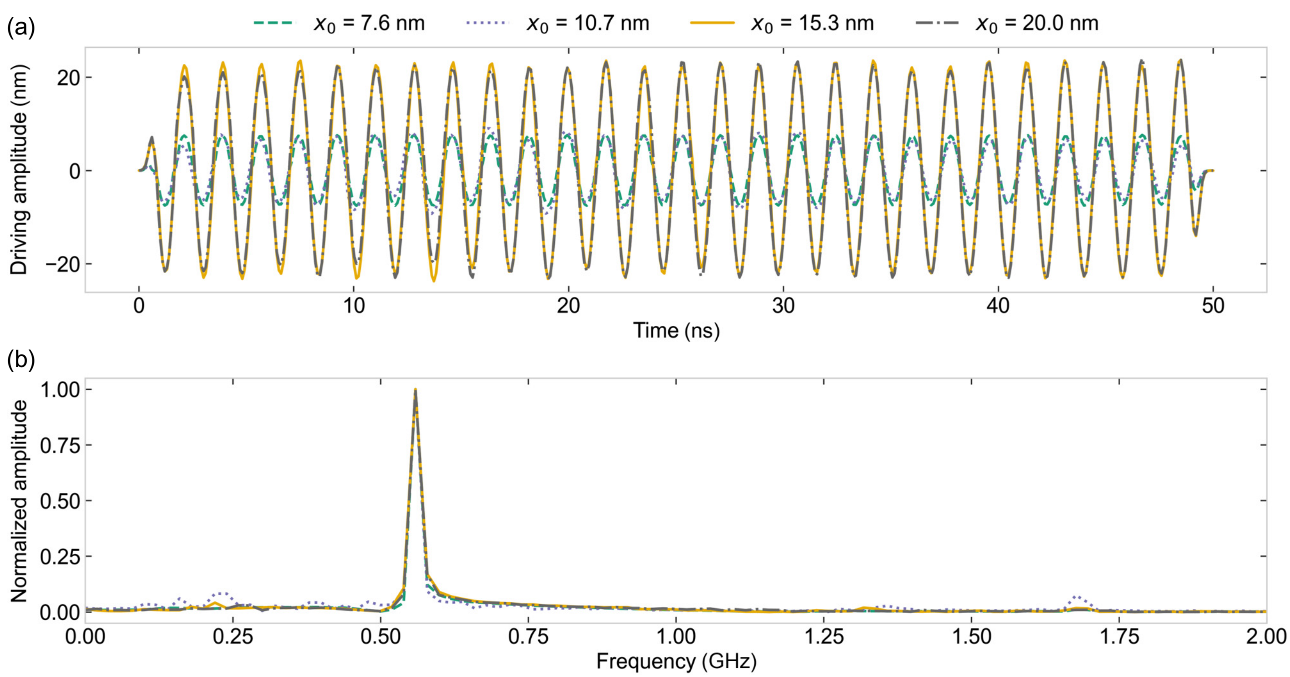

FIG. 6. (a) Optimized trajectories, and (b) corresponding single-sided amplitude spectra.

The following observations are in order. First, the obtained optimal trajectories are overall smooth, and the frequencies for all trajectories are predominantly around the spin-splitting frequency. Second, the amplitudes of the optimized trajectories are within the desired range, avoiding any additional charge noise due to the micromagnet.

[1] G. Burkard, T. D. Ladd, A. Pan, J. M. Nichol, and J. R. Petta, Semiconductor spin qubits, Rev. Mod. Phys. **95**, 025003 (2023).

[2] D. Loss and D. P. DiVincenzo, Quantum computation with quantum dots, Phys. Rev. A **57**, 120 (1998).

[3] B. Klemt, V. Elhomsy, M. Nurizzo, P. Hamonic, B. Martinez, B. Cardoso Paz, C. Spence, M. C. Dartiailh, B. Jadot, E. Chanrion, V. Thiney, R. Lethiecq, B. Bertrand, H. Niebojewski, C. Bäuerle, M. Vinet, Y.-M. Niquet, T. Meunier, and M. Urdampilleta, Electrical manipulation of a single electron spin in CMOS using a micromagnet and spin-valley coupling, npj Quantum Inf. **9**, 1 (2023).

[4] A. M. J. Zwerver, *et al.*, Qubits made by advanced semiconductor manufacturing, Nat. Electron. **5**, 184 (2022).

[5] C. B. Simmons, J. R. Prance, B. J. Van Bael, T. S. Koh, Z. Shi, D. E. Savage, M. G. Lagally, R. Joynt, M. Friesen, S. N. Coppersmith, and M. A. Eriksson, Tunable spin loading and T_1 of a silicon spin qubit measured by single-shot readout, Phys. Rev. Lett. **106**, 156804 (2011).

[6] E. Kawakami, P. Scarlino, D. R. Ward, F. R. Braakman, D. E. Savage, M. G. Lagally, M. Friesen, S. N. Coppersmith, M. A. Eriksson, and L. M. K. Vandersypen, Electrical control of a long-lived spin qubit in a Si/SiGe quantum dot, Nat. Nanotechnol. **9**, 666 (2014).

[7] R. Neumann and L. R. Schreiber, Simulation of micromagnet stray-field dynamics for spin qubit manipulation, J. Appl. Phys. **117**, 193903 (2015).

[8] J. Yoneda, K. Takeda, T. Otsuka, T. Nakajima, M. R. Delbecq, G. Allison, T. Honda, T. Kodera, S. Oda, Y. Hoshi, N. Usami, K. M. Itoh, and S. Tarucha, A quantum-dot spin qubit with coherence limited by charge noise and fidelity higher than 99.9%, Nat. Nanotechnol. **13**, 102 (2018).

[9] X. Xue, M. Russ, N. Samkharadze, B. Undseth, A. Sammak, G. Scappucci, and L. M. K. Vandersypen, Quantum logic with spin qubits crossing the surface code threshold, Nature **601**, 343 (2022).

[10] A. R. Mills, C. R. Guinn, M. J. Gullans, A. J. Sigillito, M. M. Feldman, E. Nielsen, and J. R. Petta, Two-qubit silicon quantum processor with operation fidelity exceeding 99%, Sci. Adv. **8**, eabn5130 (2022).

[11] A. Noiri, K. Takeda, T. Nakajima, T. Kobayashi, A. Sammak, G. Scappucci, and S. Tarucha, Fast universal quantum gate above the fault-tolerance threshold in silicon, Nature **601**, 338 (2022).

[12] L. M. K. Vandersypen, H. Bluhm, J. S. Clarke, A. S. Dzurak, R. Ishihara, A. Morello, D. J. Reilly, L. R. Schreiber, and M. Veldhorst, Interfacing spin qubits in quantum dots and donors—Hot, dense, and coherent, npj Quantum Inf. **3**, 1 (2017).

[13] J. M. Boter, J. P. Dehollain, J. P. Van Dijk, Y. Xu, T. Hensgens, R. Versluis, H. W. Naus, J. S. Clarke, M. Veldhorst, F. Sebastiano, and L. M. Vandersypen, Spiderweb array: A sparse spin-qubit array, Phys. Rev. Appl. **18**, 024053 (2022).

[14] M. Künne, A. Willmes, M. Oberländer, C. Gorjaew, J. D. Teske, H. Bhardwaj, M. Beer, E. Kammerloher, R. Otten, I. Seidler, R. Xue, L. R. Schreiber, and H. Bluhm, The SpinBus architecture for scaling spin qubits with electron shuttling, Nat. Commun. **15**, 4977 (2024).

[15] M. De Smet, Y. Matsumoto, A.-M. J. Zwerver, L. Tryputen, S. L. de Snoo, S. V. Amitonov, S. R. Katiraee-Far, A. Sammak, N. Samkharadze, Ö. Gül, R. N. M. Wasserman, E. Greplová, M. Rimbach-Russ, G. Scappucci, and L. M. K. Vandersypen, High-fidelity single-spin shuttling in silicon, Nat. Nanotechnol. **20**, 866 (2025).

[16] Y. Matsumoto, M. D. Smet, L. Tryputen, S. L. de Snoo, S. V. Amitonov, A. Sammak, M. Rimbach-Russ, G. Scappucci, and L. M. K. Vandersypen, Two-qubit logic and teleportation with mobile spin qubits in silicon, ArXiv:2503.15434.

[17] I. Seidler, T. Struck, R. Xue, N. Focke, S. Trellenkamp, H. Bluhm, and L. R. Schreiber, Conveyor-mode single-electron shuttling in Si/SiGe for a scalable quantum computing architecture, npj Quantum Inf. **8**, 1 (2022).

[18] V. Langrock, J. A. Krzywda, N. Focke, I. Seidler, L. R. Schreiber, and Ł. Cywiński, Blueprint of a scalable spin qubit shuttle device for coherent mid-range qubit transfer in disordered Si/SiGe/SiO_2, PRX Quantum **4**, 020305 (2023).

[19] R. Xue, M. Beer, I. Seidler, S. Humpohl, J.-S. Tu, S. Trellenkamp, T. Struck, H. Bluhm, and L. R. Schreiber, Si/SiGe QuBus for single electron information-processing devices with memory and micron-scale connectivity function, Nat. Commun. **15**, 2296 (2024).

[20] T. Struck, M. Volmer, L. Visser, T. Offermann, R. Xue, J.-S. Tu, S. Trellenkamp, Ł. Cywiński, H. Bluhm, and L. R. Schreiber, Spin-EPR-pair separation by conveyor-mode single electron shuttling in Si/SiGe, Nat. Commun. **15**, 1325 (2024).

[21] K. C. Nowack, F. H. L. Koppens, Yu. V. Nazarov, and L. M. K. Vandersypen, Coherent control of a single electron spin with electric fields, Science **318**, 1430 (2007).

[22] M. Pioro-Ladrière, T. Obata, Y. Tokura, Y.-S. Shin, T. Kubo, K. Yoshida, T. Taniyama, and S. Tarucha, Electrically driven single-electron spin resonance in a slanting Zeeman field, Nat. Phys. **4**, 776 (2008).

[23] J. Yoneda, T. Otsuka, T. Nakajima, T. Takakura, T. Obata, M. Pioro-Ladrière, H. Lu, C. J. Palmstrøm, A. C. Gossard, and S. Tarucha, Fast electrical control of single electron spins in quantum dots with vanishing influence from nuclear spins, Phys. Rev. Lett. **113**, 267601 (2014).

[24] V. N. Golovach, M. Borhani, and D. Loss, Electric-dipole-induced spin resonance in quantum dots, Phys. Rev. B **74**, 165319 (2006).

[25] J. Yoneda, T. Otsuka, T. Takakura, M. Pioro-Ladrière, R. Brunner, H. Lu, T. Nakajima, T. Obata, A. Noiri, C. J. Palmstrøm, A. C. Gossard, and S. Tarucha, Robust micromagnet design for fast electrical manipulations of single spins in quantum dots, Appl. Phys. Express **8**, 084401 (2015).

[26] N. I. Dumoulin Stuyck, F. A. Mohiyaddin, R. Li, M. Heyns, B. Govoreanu, and I. P. Radu, Low dephasing and robust

micromagnet designs for silicon spin qubits, Appl. Phys. Lett. **119**, 094001 (2021).

[27] F. A. Zwanenburg, A. S. Dzurak, A. Morello, M. Y. Simmons, L. C. L. Hollenberg, G. Klimeck, S. Rogge, S. N. Coppersmith, and M. A. Eriksson, Silicon quantum electronics, Rev. Mod. Phys. **85**, 961 (2013).

[28] M. Veldhorst, R. Ruskov, C. H. Yang, J. C. C. Hwang, F. E. Hudson, M. E. Flatté, C. Tahan, K. M. Itoh, A. Morello, and A. S. Dzurak, Spin-orbit coupling and operation of multivalley spin qubits, Phys. Rev. B **92**, 201401 (2015).

[29] R. Ferdous, E. Kawakami, P. Scarlino, M. P. Nowak, D. R. Ward, D. E. Savage, M. G. Lagally, S. N. Coppersmith, M. Friesen, M. A. Eriksson, L. M. K. Vandersypen, and R. Rahman, Valley dependent anisotropic spin splitting in silicon quantum dots, npj Quantum Inf. **4**, 1 (2018).

[30] R. Ruskov, M. Veldhorst, A. S. Dzurak, and C. Tahan, Electron g-factor of valley states in realistic silicon quantum dots, Phys. Rev. B **98**, 245424 (2018).

[31] B. P. Wuetz, M. P. Losert, S. Koelling, L. E. A. Stehouwer, A.-M. J. Zwerver, S. G. J. Philips, M. T. Mądzik, X. Xue, G. Zheng, M. Lodari, S. V. Amitonov, N. Samkharadze, A. Sammak, L. M. K. Vandersypen, R. Rahman, S. N. Coppersmith, O. Moutanabbir, M. Friesen, and G. Scappucci, Atomic fluctuations lifting the energy degeneracy in Si/SiGe quantum dots, Nat. Commun. **13**, 7730 (2022).

[32] M. Friesen, S. Chutia, C. Tahan, and S. N. Coppersmith, Valley splitting theory of SiGe/Si/SiGe quantum wells, Phys. Rev. B **75**, 115318 (2007).

[33] M. P. Losert, M. Oberländer, J. D. Teske, M. Volmer, L. R. Schreiber, H. Bluhm, S. Coppersmith, and M. Friesen, Strategies for enhancing spin-shuttling fidelities in Si/SiGe quantum wells with random-alloy disorder, PRX Quantum **5**, 040322 (2024).

[34] J. R. F. Lima and G. Burkard, Partial Landau-Zener transitions and applications to qubit shuttling, Phys. Rev. B **111**, 235439 (2025).

[35] A. David, A. M. Pazhedath, L. R. Schreiber, T. Calarco, H. Bluhm, and F. Motzoi, Long distance spin shuttling enabled by few-parameter velocity optimization, ArXiv:2409.07600.

[36] Y. Oda, M. P. Losert, and J. P. Kestner, Suppressing Si valley excitation and valley-induced spin dephasing for long-distance shuttling, ArXiv:2411.11695.

[37] C. V. Meinersen, D. Fernandez-Fernandez, G. Platero, and M. Rimbach-Russ, Unifying adiabatic state-transfer protocols with (α, β)-hypergeometries, ArXiv:2504.08031.

[38] M. J. Rančić and G. Burkard, Electric dipole spin resonance in systems with a valley-dependent g factor, Phys. Rev. B **93**, 205433 (2016).

[39] N. Khaneja, T. Reiss, C. Kehlet, T. Schulte-Herbrüggen, and S. J. Glaser, Optimal control of coupled spin dynamics: Design of NMR pulse sequences by gradient ascent algorithms, J. Magn. Reson. **172**, 296 (2005).

[40] J. Bradbury, R. Frostig, P. Hawkins, M. J. Johnson, C. Leary, D. Maclaurin, G. Necula, A. Paszke, J. VanderPlas, S. Wanderman-Milne, and Q. Zhang, JAX: Composable transformations of Python+NumPy programs, 2018, https://github.com/google/jax.

[41] P. Virtanen, *et al.*, SciPy 1.0: Fundamental algorithms for scientific computing in Python, Nat. Methods **17**, 261 (2020).

[42] F. Motzoi, J. M. Gambetta, S. T. Merkel, and F. K. Wilhelm, Optimal control methods for rapidly time-varying Hamiltonians, Phys. Rev. A **84**, 022307 (2011).

[43] M. A. Nielsen, A simple formula for the average gate fidelity of a quantum dynamical operation, Phys. Lett. A **303**, 249 (2002).

[44] S. Sheldon, L. S. Bishop, E. Magesan, S. Filipp, J. M. Chow, and J. M. Gambetta, Characterizing errors on qubit operations via iterative randomized benchmarking, Phys. Rev. A **93**, 012301 (2016).

[45] The static dot is examined using the same physical model as that used for the electron shuttler, and the valley splitting is an order of magnitude less (around 50 μeV) than the experimental setting (around 140 μeV), where 99.9% fidelity gates where demonstrated. The impact of valley phases for the static-dot case might limit the fidelities in the simulation as compared with the experimental result. In any case, the optimized pulses perform close to the experimentally observed fidelity. The observation about shuttling performing better in terms of charge noise remains unaffected.

[46] R. Hanson, L. P. Kouwenhoven, J. R. Petta, S. Tarucha, and L. M. K. Vandersypen, Spins in few-electron quantum dots, Rev. Mod. Phys. **79**, 1217 (2007).

[47] S. N. Shevchenko, S. Ashhab, and F. Nori, Landau–Zener–Stückelberg interferometry, Phys. Rep. **492**, 1 (2010).

[48] R. Garnett, *Bayesian Optimization* (Cambridge University Press, Cambridge, UK, 2023).

[49] T. Head, M. Kumar, H. Nahrstaedt, G. Louppe, and I. Shcherbatyi, Scikit-optimize/scikit-optimize, Zenodo, 2021, https://doi.org/10.5281/zenodo.5565057.

[50] A. G. Fowler, M. Mariantoni, J. M. Martinis, and A. N. Cleland, Surface codes: Towards practical large-scale quantum computation, Phys. Rev. A **86**, 032324 (2012).

[51] J. M. Taylor, H.-A. Engel, W. Dür, A. Yacoby, C. M. Marcus, P. Zoller, and M. D. Lukin, Fault-tolerant architecture for quantum computation using electrically controlled semiconductor spins, Nat. Phys. **1**, 177 (2005).

[52] R. Raussendorf and J. Harrington, Fault-tolerant quantum computation with high threshold in two dimensions, Phys. Rev. Lett. **98**, 190504 (2007).

[53] M. Rossignolo, T. Reisser, A. Marshall, P. Rembold, A. Pagano, P. J. Vetter, R. S. Said, M. M. Müller, F. Motzoi, T. Calarco, F. Jelezko, and S. Montangero, QuOCS: The quantum optimal control suite, Comput. Phys. Commun. **291**, 108782 (2023).

[54] S. Fauquenot, A. Sarkar, and S. Feld, Open and closed loop approaches for energy efficient quantum optimal control, Adv. Quantum Technol. (2025).

[55] L. Viola and S. Lloyd, Dynamical suppression of decoherence in two-state quantum systems, Phys. Rev. A **58**, 2733 (1998).

[56] Data repository: https://doi.org/10.5281/zenodo.16783697.